

Atmospheric Results from Super-Kamiokande

Roger Wendell, for the Super-Kamiokande collaboration

Kamioka Observatory, Institute for Cosmic Ray Research, University of Tokyo, Kamioka, Gifu, 506-1205, Japan

Abstract. Recent results from a 282 kiloton-year exposure of the Super-Kamiokande detector to atmospheric neutrinos are presented. The data when fit both by themselves and in conjunction with constraints from the T2K and reactor neutrino experiments show a weak, though insignificant, preference for the normal mass hierarchy at the level of $\sim 1\sigma$. Searches for evidence of oscillations into a sterile neutrino have resulted in limits on the parameters governing their mixing, $|U_{\mu 4}|^2 < 0.041$ and $|U_{\tau 4}|^2 < 0.18$ at 90% C.L. A similar search for an indication of Lorentz-invariance violating oscillations has yielded limits three to seven orders of magnitude more stringent than existing measurements. Additionally, analyses searching for an excess of neutrinos in the atmospheric data produced from the annihilation of dark matter particles in the galaxy and sun have placed tight limits on the cross sections governing their annihilation and scattering.

Keywords: Neutrino Oscillations, Atmospheric Neutrinos, Sterile Neutrinos, Indirect Dark Matter

PACS: 14.60.Pq, 96.50.S-, 14.60.St, 11.30.Cp, 95.35.+d

Atmospheric neutrino data at Super-Kamiokande (Super-K, SK) due to their wide variation in both energy and pathlength are sensitive to a variety of physical processes. In particular they are powerful probes of both standard neutrino oscillations and mixing induced by exotic scenarios such as sterile neutrinos or Lorentz-invariance violation. At the same time they represent the most serious background to searches for nucleon decays and neutrinos produced in the self-annihilation of DM particles gravitationally bound within the Sun or Milky Way. Recent results from Super-K for a variety of these topics are presented below. For a review of results in the modeling and use of atmospheric neutrinos the interested reader is referred to [1].

Detector and Data Set

Super-Kamiokande uses 50 kilotons of ultra-pure water contained within a 41.4 m by 39.3 m cylindrical tank located at a depth of 2700 meters water equivalent in Gifu Prefecture, Japan for its measurements. The detector is optically separated into a target volume viewed by 11,146 inward-facing 20 inch photomultiplier tubes (PMTs), which form the inner detector (ID), and an outer volume instrumented with 1,885 8 inch PMTs, that form the outer detector (OD). There is a 55 cm region between the ID and OD that is not instrumented. Cherenkov radiation produced by charged particles traveling through the detector's water is collected by the PMTs and used to reconstruct physics events.

Super-K has been in operation since 1996 and has collected neutrino data over four separate run periods in that interval. During the SK-I, SK-III, and SK-IV run periods the inner volume photocathode coverage was 40% while

during the SK-II period, which was instrumented with half the number of ID PMTs, it was 20%. After an accident in 2001 which destroyed half of the ID PMTs used during SK-I, the ID PMTs have been encased in a fiberglass reinforced plastic shell to prevent the production of shockwaves in the event of a PMT implosion. In 2008 the detector electronics were upgraded to allow all PMT hits to be recorded, resulting in operations with near zero deadtime. This upgrade marked the start of SK-IV, the current SK run period. Details of the detector construction and calibration are presented in [2].

Atmospheric neutrino data are separated into three topologically distinct categories, fully contained (FC), partially contained (PC), and upward-going muons ($U\mu$). Fully contained interactions are those in which the primary event vertex has been reconstructed within the 22.5 kiloton ID fiducial volume, defined as the volume offset from the PMT wall by two meters, and deposit little energy in the OD. These interactions are subdivided into analysis samples based upon the number of reconstructed Cherenkov rings (single- or multi-ring), the event energy (sub-GeV or multi-GeV), and the particle ID (PID) of their most energetic ring (e -like or μ -like). Further subdivisions designed to enhance the charged current (CC) interaction content of certain samples, or to separate neutrino from antineutrino interactions are also performed. Events with fiducial vertices but exiting particles causing PMT hits in the OD are classified as PC. Based upon the light deposition in the OD, PC events are subdivided into "stopping" and "through-going" topologies to indicate whether or not the ID-exiting particle stopped within the OD. Upward-going muon events are produced by neutrino interactions in the rock outside of Super-K energetic enough to enter the detector from below and deposit

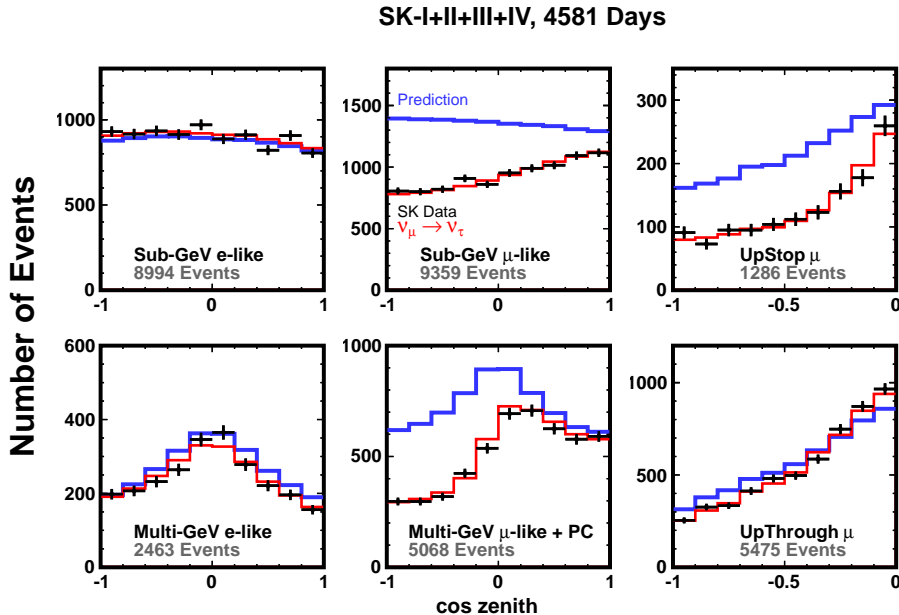


FIGURE 1. Super-K atmospheric neutrino data (points) and MC for a subset of the 19 samples used in the oscillation analysis. The MC prediction without neutrino oscillations is shown in blue and the prediction including oscillations at the analysis best fit point is shown in red.

energy in both the ID and OD. Events that traverse the entire ID volume are classified as “through-going” while those that do not are labeled “stopping.” The through-going sample is further separated into a “showering” and “non-showering” component based upon whether muon induced an electromagnetic shower within the ID. After all selections there are 19 analysis samples, some of which are shown in Figure 1.

Since the start of SK-IV it has become possible to search for the 2.2 MeV gamma ray following the capture of neutrons on protons, $p(n,\gamma)d$, in the detector water. During this period $500\mu\text{s}$ of PMT data following a physics trigger are stored to enable offline searches for these events. However, because the photons are very low energy and produce a small number of PMT hits, extracting the neutron capture signal from background events induced by radioactive contaminants is done using a neural network procedure. It should be noted though that it is not possible to completely simulate all sources of potential background at these energies, so the background model is constructed using detector data sampled using a random trigger scheme with no hit or charge requirements.

The neural network is built from 16 variables that isolate differences in the time, charge, and spatial distributions of hits originating from neutron capture events and those from backgrounds. Since most neutrons are expected to capture within 200 cm of the primary neu-

trino interaction vertex, which is required to be at least this distance from the PMT wall, variables that correlate the vertex position with the PMT activity are useful discriminants; Events from radioactive backgrounds in the detector materials may occur anywhere and often produce an isolated cluster of neighboring PMT hits, whereas neutron capture hits tend to be closer to the primary vertex with a spatial distribution that is consistent on average with the 41° Cherenkov opening angle expected from low energy electrons. This neutron tagging procedure has an estimated efficiency of 20.5% and incurs a misidentification rate of 0.018 neutrons per primary interaction. Figure 2 shows the time difference between selected neutron candidates and their primary interaction. Fitting this distribution yields a neutron capture time of $205.2 \pm 3.7\mu\text{s}$, in good agreement with existing measurements [3]. Application of this tagging to the atmospheric neutrino data set is expected to help distinguish CC antineutrino interactions, which are accompanied by a neutron at the primary vertex, from neutrino interactions and to help reduce backgrounds to proton decay searches.

Standard Oscillations

In the standard PMNS picture, atmospheric neutrino oscillations are dominated by the effects of the “atmo-

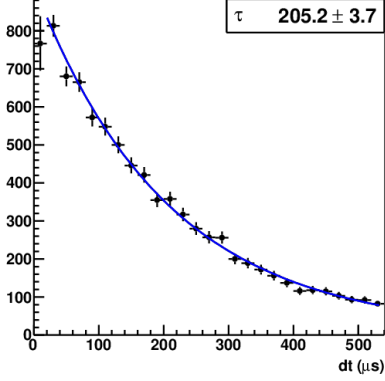


FIGURE 2. Time difference between tagged neutron capture events and their associated primary event. The blue line shows the fitted decay curve, which yields a capture lifetime of $205.2\mu\text{s}$.

spheric” mixing angle, θ_{23} , and mass splitting $\Delta m_{32,13}^2$. Broadly speaking these parameters drive oscillations of ν_μ into ν_τ and are readily seen as an absence of upward-going μ -like events in the Super-K data [4]. However, observing the appearance of one neutrino flavor among a source dominated by another provides the cleanest evidence for oscillations and has been the goal of several recent measurements [5, 6, 7]. Though in principle the detection of oscillated ν_τ events at Super-K is straightforward since there are no ν_τ in the primary atmospheric neutrino flux at the energies where oscillations are prominent, the 3.5 GeV production threshold of the τ lepton coupled with its prompt decay leads to high energy interactions with many light-producing particles that often resemble the deep inelastic scattering (DIS) interactions of the other neutrinos. For this reason extracting the ν_τ signal requires some care to disentangle it from the backgrounds.

In the Super-K analysis [8] a neural network (NN) is used to select CC ν_τ interactions in which the outgoing lepton has decayed hadronically. Though ν_τ events are expected only in the upward-going data, the downward-going data provide an important constraint on the background, which composes 96% of the events with a τ -like NN classification. As a result, a two-dimensional PDF constructed from the complete zenith angle and neural network output distributions is used to extract the τ signal. Using data from the first three Super-K run periods the analysis found $180.1 \pm 44.3(\text{stat})_{-15.2}^{+17.8}(\text{syst})$ ν_τ interactions [8]. This result is inconsistent with the hypothesis of no ν_τ appearance at the 3.8σ level.

Despite being dominated by $\nu_\mu \leftrightarrow \nu_\tau$ oscillations, oscillations with the third neutrino, ν_e , are expected to play a more important role due to the effects of θ_{13} and the Earth’s matter. Indeed, between two and 10 GeV, mat-

ter induces a resonant enhancement of the $\nu_\mu \rightarrow \nu_e$ oscillation probability for upward-going neutrinos traversing the core and mantle of the planet. Importantly, this enhancement depends both on the sign of the mass hierarchy and the CP state of the neutrino: for a normal (inverted) mass hierarchy the resonance exists for neutrinos (antineutrinos) only. Since there are both neutrinos and antineutrinos in the atmospheric flux the ability to separate the two provides enhanced hierarchy sensitivity. Even without it, the resonance effect leads to a $\sim 12\%(5\%)$ increase in the rate of both single- and multi-ring multi-GeV upward-going e -like events assuming a normal (inverted) mass hierarchy.

At these energies the increase in DIS cross section leads to complicated multi-ring event topologies. Often the PID of the primary lepton is obscured by rings from charged hadrons, making it difficult to distinguish muons from electrons. In order to purify the multi-ring sample in CC $\nu_e + \bar{\nu}_e$ interactions, events whose most energetic ring’s PID is e -like are subjected to a likelihood selection which removes CC $\nu_\mu + \bar{\nu}_\mu$ and neutral current (NC) interactions [9]. This selection provides a passing sample that is $\sim 75\%$ pure in CC $\nu_e + \bar{\nu}_e$ interactions. It should be noted though that in order to combat the effects of low statistics and to provide additional systematic error constraints on the NC and ν_τ components of the analysis samples, the rejected events are now used for the first time in the analysis. This additional sample is composed of roughly equal parts CC ν_e, ν_μ , and NC interactions, with a 5% contribution from ν_τ .

To improve sensitivity to the mass hierarchy, events in the passing sample are separated into ν_e - and $\bar{\nu}_e$ -like subsamples by a second likelihood procedure. The likelihood is constructed to exploit the expected differences in both the number of expected charged pions and the amount of transverse momentum in the respective interactions (c.f. [10]). After selection the $\nu_e(\bar{\nu}_e)$ -like sample is 59.4%(21.0%) pure in CC $\nu_e(\bar{\nu}_e)$ interactions. A similar separation, based solely on the number of Michel electrons found, is performed for multi-GeV single-ring e -like events. The respective purities after this cut are 62.8% and 36.7%.

Using these samples in conjunction with both e -like and μ -like data from the remainder of the atmospheric data set, a simultaneous fit for θ_{23} , Δm_{23}^2 , and δ_{cp} is performed for each hierarchy assumption. During these fits the value of $\sin^2\theta_{13}$ has been fixed to 0.025 based on recent measurements [11, 12, 13] but its uncertainty is included as a systematic error. The “1-2” terms are treated in a similar fashion. A total of 154 systematic errors stemming from uncertainties in the flux and cross section models, as well as the detector’s performance are included in the fit. Using the Super-K atmospheric neutrino data a weak preference for the mass hierarchy, $\chi_{IH}^2 - \chi_{NH}^2 = 0.9$, is found. Best fit information for this

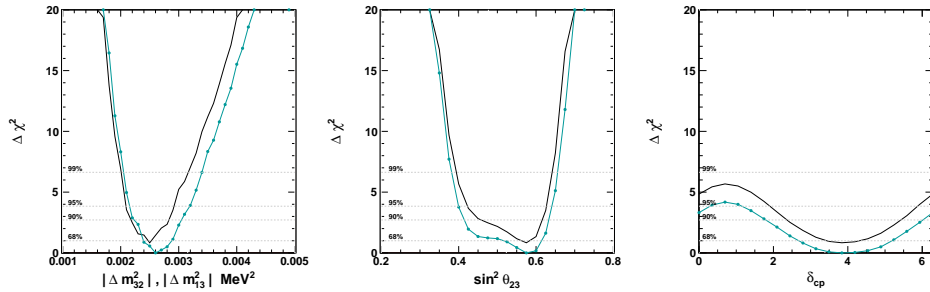


FIGURE 3. Constraints on neutrino oscillation parameters from the Super-K atmospheric neutrino data. Black lines denote the inverted hierarchy result, which has been offset from the normal hierarchy result, shown in blue, by the difference in their minimum χ^2 values.

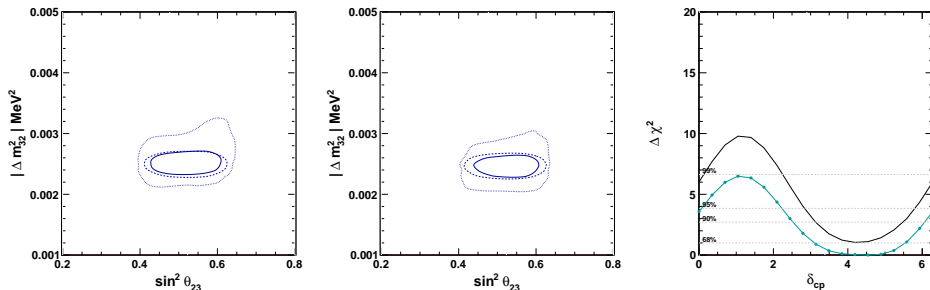


FIGURE 4. Constraints on neutrino oscillation contours from a combined fit of Super-K atmospheric neutrino data and a model of the T2K experiment. The left two figures show two dimensional constraints from the atmospheric neutrino data alone (dashed), the T2K model (dotted), and their combination (solid) for the normal and inverted hierarchy, respectively. The right figure shows the constraint on the δ_{CP} parameter from the combined fit with the inverted hierarchy fit (black) offset from the normal hierarchy fit (blue, markers) by the difference in their minimum χ^2 values.

TABLE 1. Summary of best fit information for fits assuming either the normal (NH) or inverted (IH) mass hierarchy using either the Super-K atmospheric neutrino data only (517 d.o.f.), or combining it with the T2K model (543 d.o.f.) described in the text.

Fit	χ^2_{min}	δ_{CP}	$\sin^2\theta_{23}$	$\Delta m^2_{32,13}$ [eV ²]
SK NH	559.8	3.84	0.57	2.6×10^{-3}
SK IH	560.7	3.84	0.57	2.5×10^{-3}
SK+T2K NH	578.2	4.19	0.55	2.5×10^{-3}
SK+T2K IH	579.4	4.19	0.55	2.5×10^{-3}

analysis is summarized in Table 1. One dimensional $\Delta\chi^2$ distributions for the oscillation variables are presented in Figure 3. Unfortunately, the magnitude of the resonance-enhanced oscillation probability described above carries a strong dependence on the value of $\sin^2\theta_{23}$ and is similarly modulated, though to a lesser degree, by the value of δ_{CP} . If the former is 0.6 then the expected increase in the upward going multi-GeV event e -like rate is 17% compared to 8% if it is 0.4. By using both e -like and μ -like data Super-K is able to constrain the atmospheric

mixing parameters, but since the direction of incoming atmospheric neutrino is unknown, its measurements are limited. Accordingly, the incorporation of external constraints on these parameters from more precise measurements is a means of increasing the sensitivity of the analysis.

Measurements of atmospheric mixing using accelerator neutrinos, such as those from the T2K [14] and MINOS [7] experiments, provide tight constraints on both $\sin^2\theta_{23}$ and $|\Delta m^2_{32}|$. Since the T2K experiment uses Super-K as its far detector and the event simulation and reconstruction are common between beam and atmospheric neutrino events, it is straightforward to build a model of the T2K experiment using only information in the literature and atmospheric analysis tools. It is further possible to construct systematic error correlations between the atmospheric sample and a T2K model. Though MINOS [7] provides important constraints on atmospheric mixing, notably $|\Delta m^2_{32}|$, the differences between it and Super-K make building an accurate model of the experiment more challenging. Below only a model of T2K is used to constrain the atmospheric neutrino analysis, but plans exist to extend those constraints to include

MINOS and other experiments.

A model of the T2K experiment’s ν_e appearance [5] and ν_μ disappearance [14] analysis samples has been constructed using atmospheric neutrino tools. Using published beam flux information [15] atmospheric neutrino MC are reweighted to produce a beam MC. The beam MC is subjected to the same selection criterion outlined in the references to produce model ν_e and ν_μ samples. Data are digitized from the references. T2K has published estimates of its systematic errors in terms of changes in the sample event rates and these have been recast into the Super-K style of systematic error treatment (c.f. [9]). Due to its low statistics and for ease of analysis only one analysis bin is used for the model ν_e sample; For the model ν_μ sample the same binning as the reference is used.

After construction of the systematic errors and analysis samples, independent fits of each model sample were performed to verify the model reproduced the same parameter constraints as T2K’s published results. These samples are then fit together with the 19 Super-K analysis samples, assuming full correlation between relevant systematic error parameters, such as those in the cross section model. Contours from the combined fit are presented in Figure 4 and the best fit information is listed in Table 1. After inclusion of the T2K model, the preference for the normal mass hierarchy improved slightly to $\chi_{IH}^2 - \chi_{NH}^2 = 1.2$, but remains insignificant. Though a preference is seen in both the Super-K and combined analysis for $\delta_{cp} \sim 3\pi/2$ CP-conservation is allowed at at least the 90% confidence level.

Exotic Mixing Scenarios

Though the standard paradigm of neutrino oscillations driven by two mass differences, $\Delta m_{12}^2 \sim 10^{-5} \text{eV}^2$ and $\Delta m_{32}^2 \sim 10^{-3} \text{eV}^2$, is well established, there are a number of experimental hints for a third mass difference, $\Delta m_s^2 \sim 1 \text{eV}^2$ (c.f. [18, 19, 20, 21]) that does not fit into this picture. Based on constraints from measurements of the Z^0 decay width, it is known that the existence of a fourth (or higher) neutrino state to explain these hints implies that it does not participate in the weak interaction. It is therefore termed “sterile.” If there are oscillations into such a state, its lack of interaction can induce reductions and spectral distortions in the atmospheric neutrino flux at Super-K.

As an interferometric effect atmospheric neutrino oscillations are similarly sensitive to Lorentz-invariance violation (LV). While there is currently no evidence for the violation of this symmetry, its fundamental role in both the standard model of particle physics and general relativity make it the target of critical experimental investiga-

TABLE 2. Summary of best fit information for sterile neutrino oscillations for fits assuming either no ν_e oscillations or lack of sterile matter effects (Sterile_{vacuum}). Best fits as well as limits at 90% C.L. are shown. The minimum χ^2 for the No- ν_e and Sterile_{vacuum} fits was 531.1 and 532.1 for 480 d.o.f., respectively.

Fit	$ U_{\mu 4} _{best}^2$	$ U_{\tau 4} _{best}^2$	$ U_{\mu 4} _{lim}^2$	$ U_{\tau 4} _{lim}^2$
No- ν_e	0.012	0.021	–	< 0.18
Sterile _{vacuum}	0.016	–	< 0.041	–

tion. Indeed, an observation of LV would provide access to Planck scale physics [22, 23, 24], an energy scale far out of reach of collider experiments. In this section analyses searching for these types of exotic oscillation effects are presented.

Sterile Neutrino Oscillations

Atmospheric neutrinos can provide useful constraints on mixing into sterile states as they are essentially insensitive to the exact number of sterile neutrinos and for $\Delta m_s^2 > 0.1 \text{eV}^2$ the oscillations are sufficiently fast that they are insensitive to the precise value of the mass splitting. In general, the addition of sterile states to standard PMNS oscillations leads to a mixing matrix of the following form,

$$U = \begin{pmatrix} U_{e1} & U_{e2} & U_{e3} & U_{e4} & \cdots \\ U_{\mu 1} & U_{\mu 2} & U_{\mu 3} & U_{\mu 4} & \cdots \\ U_{\tau 1} & U_{\tau 2} & U_{\tau 3} & U_{\tau 4} & \cdots \\ U_{s1} & U_{s2} & U_{s3} & U_{s4} & \cdots \\ \vdots & \vdots & \vdots & \vdots & \ddots \end{pmatrix}, \quad (1)$$

where ellipses denote entries for models with more than one additional state. Further, since sterile neutrinos do not experience NC interactions they are subject to an additional effective potential,

$$V_s = \pm(G_F/\sqrt{2})\text{diag}(0,0,0,N_n,\dots), \quad (2)$$

when traveling through matter which is not felt by the active neutrinos. Here N_n is the local neutron density and G_F the Fermi constant. To simplify the oscillation computations the number of sterile states is taken to be one and it is assumed there is no $\nu_e \leftrightarrow \nu_s$ mixing, i.e. $U_{e4} = 0$. In this context oscillation probabilities for the analyses below have been calculated based on [25].

The analysis is divided into two pieces based on two approximations with different domains of applicability. In the first analysis, it is assumed that there is no mixing between ν_e and the other active neutrinos, that is $\theta_{13} = \theta_{23} = 0$. Under this approximation atmospheric

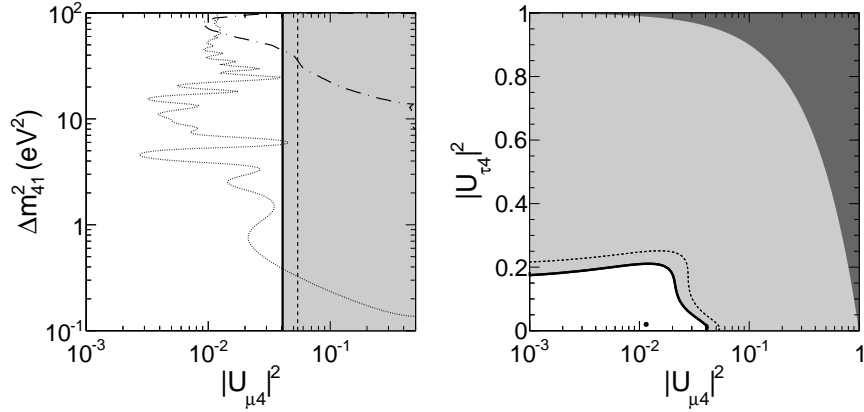


FIGURE 5. Constraints on sterile neutrino oscillations assuming the neutron density in the Earth is zero (left) and ν_e s do not participate in any oscillations (right). The solid (dashed) line indicates the 90% (99%) limit with the exclusion region shaded in gray. Limits at 90% C.L. from a joint analysis of MiniBooNE and SciBooNE data [16] as well as from the CCFR experiment [17] appear as the dotted and dash-dot curves, respectively.

neutrinos are sensitive to both $|U_{\mu 4}|$ and $|U_{\tau 4}|$ at the expense of providing a slightly biased estimate of the former. Since $|U_{\mu 4}|$ decreases the overall ν_μ survival probability and therefore produces a reduction in the normalization of the μ -like samples, their correlation with the e -like samples through systematic uncertainties in the flux model ultimately leads to a bias towards lower values of this parameter, due to the now missing θ_{13} -induced e -like events discussed above. Constraints on $|U_{\tau 4}|$ are nonetheless possible as it introduces distortions in the shape of the higher energy ν_μ -rich PC and Up μ samples through the sterile matter effect. The second analysis assumes regular PMNS mixing with a sterile neutrino but takes the neutron matter density to be zero. While this assumption removes the effects of matter on sterile neutrino oscillations, it allows for an unbiased measure of $|U_{\mu 4}|$.

Both analyses use 18 of the 19 Super-K analysis samples for a total of 480 degrees of freedom. Standard oscillation parameters are unvaried in the fit and have been fixed to $\Delta m_{32}^2 = 2.51 \pm 0.10 \times 10^{-3} \text{eV}^2$, $\sin^2 \theta_{23} = 0.514 \pm 0.055$, $\sin^2 2\theta_{13} = 0.095 \pm 0.01$, $\Delta m_{21}^2 = 7.46 \pm 0.19 \times 10^{-5} \text{eV}^2$, $\sin^2 \theta_{12} = 0.305 \pm 0.021$, with $\delta_{cp} = 0$ and assuming a normal mass hierarchy. The quoted uncertainties are treated as systematic errors during the fit for the sterile mixing parameters. After performing fits to both of the oscillation scenarios no evidence for oscillations with $\Delta m_s^2 \sim 1 \text{eV}^2$ nor for spectral distortions induced by sterile matter effects is found. Limits placed on the sterile mixing parameters as well as best fit information is summarized in Table 2. Allowed regions from the two analyses appear in Figure 5.

Lorentz Violation in Neutrino Oscillations

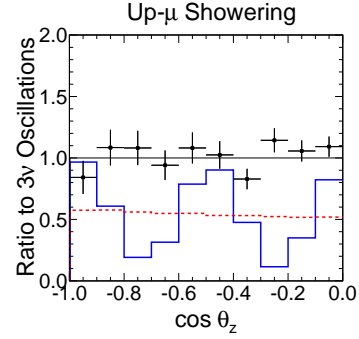


FIGURE 6. Illustration of the effects of LV on neutrino oscillations for the the Up μ showering sample. Data points are shown relative to the prediction from standard oscillations as a function of zenith angle. The ratio of LV oscillations to standard oscillations is shown in blue (red) for $a_{\mu\tau}^T = 10^{-22} \text{GeV}$ ($c_{\mu\tau}^{TT} = 10^{-22}$).

The effects of LV on atmospheric neutrinos may manifest as sidereal variations in their oscillations or as distortions in the oscillated spectra [26, 27, 28]. Super-K has undergone a search for the latter within the framework of the standard model extension (SME) [24], an observer independent effective field theory which contains the standard model, general relativity, and all possible LV operators. Within the SME the usual Hamiltonian describing

neutrino propagation appears with a LV component,

$$H_{LV} = \begin{pmatrix} 0 & a_{e\mu}^T & a_{e\tau}^T \\ (a_{e\mu}^T)^* & 0 & a_{\mu\tau}^T \\ (a_{e\tau}^T)^* & (a_{\mu\tau}^T)^* & 0 \end{pmatrix} - E \begin{pmatrix} 0 & c_{e\mu}^{TT} & c_{e\tau}^{TT} \\ (c_{e\mu}^{TT})^* & 0 & c_{\mu\tau}^{TT} \\ (c_{e\tau}^{TT})^* & (c_{\mu\tau}^{TT})^* & 0 \end{pmatrix}, \quad (3)$$

where $a_{\alpha\beta}^T$ and $c_{\alpha\beta}^{TT}$ are complex coefficients for isotropic LV operators. Generally the $a_{\alpha\beta}^T$ parameters produce oscillation effects proportional to the neutrino propagation distance, L , while the $c_{\alpha\beta}^{TT}$ induce effects that depend on LE , where E is the neutrino energy. Given the form of these effects, the large variation in atmospheric neutrino pathlengths (from ~ 10 to 13,000 km) and energy (from 100 MeV to 10 TeV and above) make them particularly sensitive probes. However, it is for precisely this reason that perturbative approaches such as [29] cannot be used and the full SME Hamiltonian must be diagonalized. Accordingly, oscillation probabilities for the analysis below have been obtained following [30].

The effects on neutrino oscillations from even modest amounts of LV can be dramatic and generally appear in the multi-GeV (both e -like and μ -like), PC, and Up μ samples. As an example, Figure 6 shows the ratio of the zenith angle distribution of the Up μ showering data, whose events have both long flight lengths and the highest energy of the Super-K samples, relative to the expectation assuming standard oscillations. A blue (red) line shows the effect of LV oscillations as the same ratio using the MC prediction assuming $a_{\mu\tau}^T = 10^{-22}$ GeV ($c_{\mu\tau}^{TT} = 10^{-22}$), both of which show large departures from standard oscillations. In the search for LV in the atmospheric neutrino data the standard oscillation parameters are held fixed at the same values used in the sterile oscillation search above, with the exception of δ_{cp} , which is allowed to vary freely in the fit. Each LV coefficient is then fit for both its real and imaginary components while holding all other LV parameters at zero. The results are listed in Table 3. No evidence for LV has been seen in any of the fits and has resulted both in limits three to seven orders of magnitude stronger than existing measurements [31, 32] and has also established new limits, in particular on the $a_{\mu\tau}^T$ and $c_{\mu\tau}^{TT}$ parameters.

Indirect WIMP Searches

While atmospheric neutrinos have been primarily discussed in the context of a signal source in the above, they also serve as a background to searches for rare phenomena such as nucleon decays and dark matter (DM) annihilation into neutrinos. Indeed, weakly interacting mas-

TABLE 3. Summary of the results of the six fits for Lorentz-violating parameters where the real and imaginary parts of each parameter are fit simultaneously. The best fit parameters and their 95% upper limits are shown.

LV Parameter	Best Fit	95% Upper Limit	
$e\mu$	Re(a^T)	1.0×10^{-23} GeV	1.8×10^{-23} GeV
	Im(a^T)	4.6×10^{-24} GeV	1.8×10^{-23} GeV
	Re(c^{TT})	1.0×10^{-28}	1.1×10^{-26}
	Im(c^{TT})	1.0×10^{-28}	1.1×10^{-26}
$e\tau$	Re(a^T)	2.2×10^{-24} GeV	4.1×10^{-23} GeV
	Im(a^T)	1.0×10^{-28} GeV	2.8×10^{-23} GeV
	Re(c^{TT})	1.0×10^{-28}	1.2×10^{-24}
	Im(c^{TT})	4.6×10^{-25}	1.4×10^{-24}
$\mu\tau$	Re(a^T)	3.2×10^{-24} GeV	6.5×10^{-24} GeV
	Im(a^T)	1.0×10^{-28} GeV	5.1×10^{-24} GeV
	Re(c^{TT})	1.0×10^{-28}	5.8×10^{-27}
	Im(c^{TT})	1.0×10^{-27}	5.6×10^{-27}

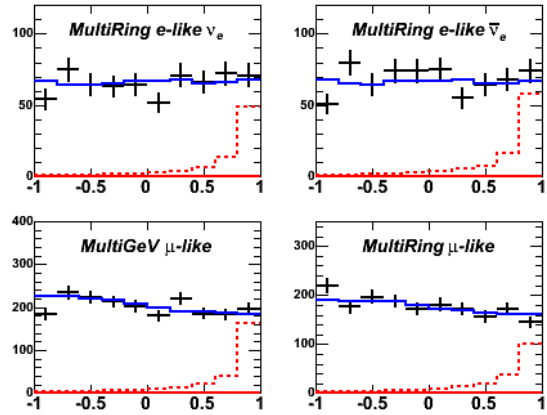


FIGURE 7. Illustration of the expected signal at Super-K from 5 GeV WIMP annihilation around the galactic center. The horizontal axis shows the cosine of the angle to the galactic center. Data, atmospheric background MC, and the WIMP signal appear as the markers, blue line, and red dashed line, respectively. Though the analysis uses 18 analysis samples for the fit, only the four particularly relevant to this channel are shown. The signal normalization has been exaggerated for visibility.

sive particles, WIMPs, are a promising candidate for cold dark matter as the weakness of their interactions provides a natural explanation of the relic abundance of DM [33, 34, 35]. If such particles exist it is possible that their annihilation or decays could produce standard model particles, such as neutrinos or particles whose decay chains include neutrinos. In this scenario large gravitational potentials, such as the Milky Way or the Sun, can trap WIMPs, providing an arena for their collisions. The existence of such a source would manifest in Super-

K atmospheric neutrino data as a neutrino excess coming from a particular direction on the sky, with energies as large as the WIMP mass. Searches for evidence of WIMP annihilation in the Sun and the galactic center (GC) are described here.

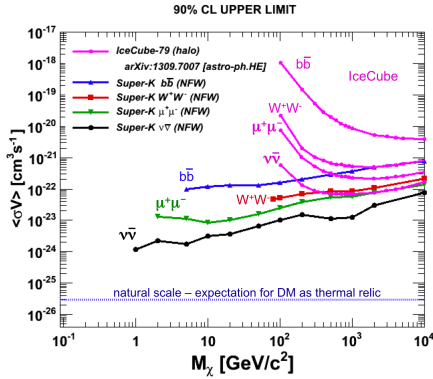


FIGURE 8. Upper limits on the WIMP self-annihilation cross section averaged over the density distribution found in [36] for various assumed masses and annihilation modes. Limits from the IceCube experiment [37] are also shown in pink.

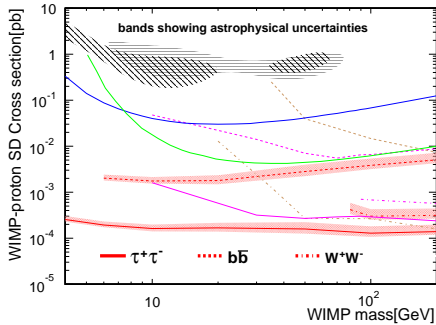


FIGURE 9. Upper limits on the SD WIMP-proton cross section calculated using DarkSUSY [38]. The 90% C.L. limits for the Super-K results are: $\tau^+\tau^-$ (red solid), $b\bar{b}$ (red dashed); W^+W^- (red dot-dashed). The bands around each limit indicate the uncertainty in the assumed solar model and velocity distribution. Also shown are limits from other experiments: IceCube [39] $b\bar{b}$ (brown dashed) / W^+W^- (brown dot-dashed); BAKSAN [40] $\tau^+\tau^-$ (pink solid) / $b\bar{b}$ (pink dashed) / W^+W^- (pink dot-dashed); PICASSO [41] (blue solid); SIMPLE [42] (green solid). The black shaded regions are the 3σ C.L. signal claimed by DAMA/LIBRA [43, 44].

WIMP annihilation into several channels is considered. For annihilation in the GC these channels are $\chi\chi \rightarrow W^+W^-, b\bar{b}, \mu^+\mu^-$ and $\nu\bar{\nu}$, and for annihilation in the Sun they are $\chi\chi \rightarrow W^+W^-, b\bar{b}, \tau^+\tau^-$. Due to the strong directionality of the expected signal, these analyses are binned in both momentum as well as the cosine of the direction to the GC (Sun). Figure 7 shows an illustration of the expected signal at Super-K for 5 GeV WIMP annihilation overlaid with the data and MC assuming standard

oscillations. The horizontal axis shows the cosine of the direction to the GC and the signal normalization is arbitrary. Though the atmospheric neutrino data and MC distribution do not peak towards the GC, the simulated WIMP signal does; this feature allows for powerful constraints on a potential signal. For annihilation in the Sun the plots look similar, though the direction coordinate is different.

The analyses are performed by assuming several potential WIMP masses ranging from a few to several hundred GeV and separately assuming a 100% branching ratio into each of the annihilation channels above. During the fit the signal and atmospheric neutrino background normalizations are simultaneously varied to achieve the best agreement with the data. No evidence for an excess of WIMP-induced neutrinos is found in either analysis. As a result, for the GC analysis, limits are placed on the velocity averaged WIMP self-annihilation cross section using the DM density distribution given by [36]. Figure 8 shows the 90% C.L. upper bounds on this parameter for a variety of annihilation channels and assumed dark matter masses.

By making assumptions about the composition of the Sun and the velocity distribution of WIMPs trapped in its gravitational potential, it is possible to extract limits on both the WIMP spin-dependent (SD) and spin-independent (SI) scattering cross section on nuclei. Assuming that the capture rate of WIMPs is in equilibrium with their annihilation rate, that they populate a DM halo with local density 0.3 GeV/cm^3 [45, 46] with an RMS velocity of 270 km/s, and that the solar rotation speed is of 220 km/s, the SD limits appearing Figure 9 have been obtained. Note that these are the most stringent constraint on the SD cross section for WIMP mass less than $200 \text{ GeV}/c^2$ assuming 100% annihilation into $\tau^+\tau^-$. This analysis also places stringent limits on the SI cross section. For instance, the 90% C.L. limits on $\chi\chi \rightarrow b\bar{b}$ and $\chi\chi \rightarrow \tau^+\tau^-$ are $240 \times 10^{-43} \text{ cm}^2$ and $21.2 \times 10^{-43} \text{ cm}^2$, respectively. These results are in tension with the findings of CDMS II [47] and to a lesser extent with CoGeNT [48] and CRESSTII [49].

Conclusion

Super-K atmospheric neutrino data have been studied in the context of both standard and exotic oscillation scenarios as well as in the search for neutrinos produced in the annihilation of WIMPs in our galactic halo and Sun. Atmospheric neutrino constraints on standard mixing remain compelling and thus far have a weak, $\sim 1\sigma$ preference for the normal mass hierarchy. While this result remains statistically limited, efforts to improve sensitivity by introducing constraints from external experiments have yielded similar conclusions. Though no evidence

for the existence of sterile or LV oscillations is found in the data, stringent limits on the parameters governing both have been obtained. Finally, searches for an excess of neutrinos coming from the direction of the galactic center and the Sun, have resulted in tight constraints, in particular at low masses, on the WIMP's velocity averaged self-annihilation cross section as well as its scattering cross sections on nuclei.

ACKNOWLEDGMENTS

The author would like to thank the organizers for the opportunity to present these results. The Super-Kamiokande collaboration gratefully acknowledges the cooperation of the Kamioka Mining and Smelting Company. Super-K has been built and operated from funds provided by the Japanese Ministry of Education, Culture, Sports, Science and Technology, the U.S. Department of Energy, and the U.S. National Science Foundation. This work was partially supported by the Research Foundation of Korea (BK21 and KNRC), the Korean Ministry of Science and Technology, the National Science Foundation of China, the European Union FP7 (DS laguna-lbno PN-284518 and ITN invisibles GA-2011-289442) the National Science and Engineering Research Council (NSERC) of Canada, and the Scinet and Westgrid consortia of Compute Canada.

REFERENCES

1. T. Kajita, *New J.Phys.* **6**, 194 (2004).
2. K. Abe, Y. Hayato, T. Iida, K. Iyogi, J. Kameda, et al., *Nucl.Instrum.Meth.* **A737**, 253–272 (2014), 1307.0162.
3. D. Cokinos, and E. Melkonian, *Phys.Rev.* **C15**, 1636–1643 (1977).
4. K. Abe, et al., *Phys.Rev.Lett.* **107**, 241801 (2011), 1109.1621.
5. K. Abe, et al., *Phys.Rev.Lett.* **112**, 061802 (2014), 1311.4750.
6. N. Agafonova, et al., *JHEP* **1311**, 036 (2013), 1308.2553.
7. P. Adamson, et al., *Phys.Rev.Lett.* **112**, 191801 (2014), 1403.0867.
8. K. Abe, et al., *Phys.Rev.Lett.* **110**, 181802 (2013), 1206.0328.
9. R. Wendell, et al., *Phys.Rev.* **D81**, 092004 (2010), 1002.3471.
10. Ka Pik Lee, *Study of the neutrino mass hierarchy with the atmospheric neutrino data observed in Super-Kamiokande*, Ph.D. thesis, The University of Tokyo (2012).
11. F. An, et al., *Chin.Phys.* **C37**, 011001 (2013), 1210.6327.
12. J. Ahn, et al., *Phys.Rev.Lett.* **108**, 191802 (2012), 1204.0626.
13. Y. Abe, et al., *Phys.Rev.Lett.* **108**, 131801 (2012), 1112.6353.
14. K. Abe, et al., *Phys. Rev. Lett.* **111**, 211803 (2013), 1308.0465.
15. K. Abe, et al., *Phys.Rev.* **D87**, 012001 (2013), 1211.0469.
16. G. Cheng, et al., *Phys.Rev.* **D86**, 052009 (2012), 1208.0322.
17. I. E. Stockdale, A. Bodek, F. Borcherding, N. Giokaris, K. Lang, et al., *Phys.Rev.Lett.* **52**, 1384 (1984).
18. A. Aguilar, et al., *Phys.Rev.* **D64**, 112007 (2001), hep-ex/0104049.
19. A. A. Aguilar-Arevalo, et al., *Phys.Rev.Lett.* **110**, 161801 (2013).
20. P. Huber, *Phys.Rev.* **C84**, 024617 (2011), 1106.0687.
21. G. Mention, M. Fechner, T. Lasserre, T. Mueller, D. Lhuillier, et al., *Phys.Rev.* **D83**, 073006 (2011), 1101.2755.
22. D. Colladay, and V. A. Kostelecky, *Phys.Rev.* **D55**, 6760–6774 (1997), hep-ph/9703464.
23. D. Colladay, and V. A. Kostelecky, *Phys.Rev.* **D58**, 116002 (1998), hep-ph/9809521.
24. V. A. Kostelecky, *Phys.Rev.* **D69**, 105009 (2004), hep-th/0312310.
25. M. Maltoni, and T. Schwetz, *Phys.Rev.* **D76**, 093005 (2007).
26. A. Kostelecky, and M. Mewes, *Phys.Rev.* **D85**, 096005 (2012), 1112.6395.
27. V. A. Kostelecky, and M. Mewes, *Phys.Rev.* **D70**, 031902 (2004), hep-ph/0308300.
28. V. A. Kostelecky, and M. Mewes, *Phys.Rev.* **D69**, 016005 (2004), hep-ph/0309025.
29. J. S. Diaz, V. A. Kostelecky, and M. Mewes, *Phys.Rev.* **D80**, 076007 (2009), 0908.1401.
30. J. S. Diaz (2014), in preparation, IUHET 585.
31. T. Katori, *Mod.Phys.Lett.* **A27**, 1230024 (2012), 1206.6915.
32. T. Katori, and J. Spitz, “Testing Lorentz Symmetry with the Double Chooz Experiment,” in *CPT and Lorentz Symmetry VI*, World Scientific, Singapore, 2014, 1307.5805.
33. G. Steigman, and M. S. Turner, *Nucl.Phys.* **B253**, 375 (1985).
34. G. Jungman, M. Kamionkowski, and K. Griest, *Phys.Rept.* **267**, 195–373 (1996), hep-ph/9506380.
35. G. Bertone, D. Hooper, and J. Silk, *Phys.Rept.* **405**, 279–390 (2005), hep-ph/0404175.
36. J. F. Navarro, C. S. Frenk, and S. D. White, *Astrophys.J.* **462**, 563–575 (1996), astro-ph/9508025.
37. M. Aartsen, et al. (2013), 1309.7007.
38. P. Gondolo, J. Edsjo, P. Ullio, L. Bergstrom, M. Schelke, et al., *JCAP* **0407**, 008 (2004).
39. M. G. Aartsen, et al., *Phys.Rev.Lett.* **110**, 131302 (2013).
40. M. M. Boliev, S. V. Demidov, S. P. Mikheyev, and O. V. Suvorova, *JCAP* **1309**, 019 (2013).
41. S. Archambault, et al., *Phys.Lett.* **B711**, 153–161 (2012).
42. M. Felizardo, T. A. Girard, T. Morlat, A. C. Fernandes, A. R. Ramos, et al., *Phys.Rev.Lett.* **108**, 201302 (2012).
43. R. Bernabei, et al., *Eur.Phys.J.* **C56**, 333–355 (2008).
44. C. Savage, G. Gelmini, P. Gondolo, and K. Freese, *JCAP* **0904**, 010 (2009).
45. M. Kamionkowski, and A. Kinkhabwala, *Phys.Rev.* **D57**, 3256–3263 (1998).

46. W. M. Yao, et al., *J.Phys.* **G33**, 1–1232 (2006).
47. R. Agnese, et al., *Phys.Rev.Lett.* **111**, 251301 (2013).
48. C. E. Aalseth, et al., *Phys.Rev.Lett.* **106**, 131301 (2011).
49. G. Angloher, M. Bauer, I. Bavykina, A. Bento, C. Bucci, et al., *Eur.Phys.J.* **C72**, 1971 (2012).